Photon Energy Dependent Ultrafast Photo-Induced THz Response in Microcrystalline Film of $CH_3NH_3PbBr_3$

Hiroto Okochi,[†] Hiroyuki Katsuki,[*,†,‡] Masaaki Tsubouchi,[*,¶] Ryuji Itakura,[¶] and Hisao Yanagi[§]

†*Graduate School of Advanced Science and Technology, Nara Institute of Science and Technology, Ikoma 630-0192 JAPAN*

‡*Department of Photo-molecular Science, Institute for Molecular Science, National Institutes of Natural Sciences, Okazaki 444-8585 JAPAN*

¶*National Institutes for Quantum and Radiological Science and Technology (QST), Kansai Photon Science Institute, Kizugawa 619-0215 JAPAN*

§*Graduate School of Advanced Science and Technology,, Nara Institute of Science and Technology, Ikoma 630-0192 JAPAN*

E-mail: katsuki@ms.naist.jp; tsubouchi.masaaki@qst.go.jp

Abstract

Time-resolved terahertz (THz) spectroscopy is applied for a microcrystalline film of methylammonium lead bromide perovskite, $CH_3NH_3PbBr_3$, to observe the carrier dynamics around the band edge. The ultrafast response of the transmitted THz electric field amplitude after the carrier generation is modeled with a bi-exponential curve with $\sim$ 5 ps and 180 ps time constants, which are ascribed to Auger and electron-hole recombination processes, respectively. From the pump photon energy dependence of the time evolution of the THz electric field amplitude, it is shown that the bound exciton states and free inter-band excited carrier states show clearly different temporal response. These measurements support that the bound excitons generated in $CH_3NH_3PbBr_3$ stay as stable excitons even at room temperature (RT). This is in clear contrast to the cases in $CH_3NH_3PbI_3$ where the excitons and band-edge free carriers are interchangeable at RT.

Graphical TOC Entry

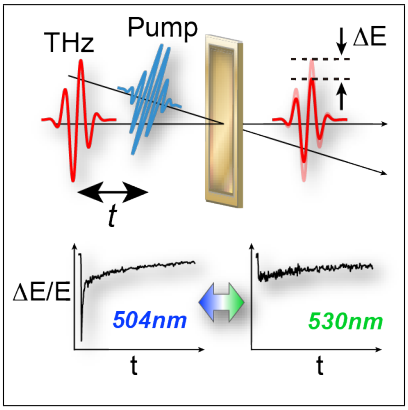

Hybrid organic-inorganic lead halide perovskites (HOIPs) have been widely studied in various research fields ranging from solar cell applications[1,2] to organic lasers[3–6] and light emitting diodes.[7–9] Their noteworthy properties such as long carrier lifetime, high tolerance for defects, and the band gap tunability by mixing halide atoms set HOIPs promising candidates for the future opto-electronic applications. In the recent report, the power conversion efficiency over 25% has been reported with a tandem solar cell with HOIP used as active layers.[10] As for nano-photonic application, low threshold lasing with 220 nJ/cm^2 pump fluence has been reported with nanowire structure under optical excitation.[3] For the further improvement and development of HOIP-based photovoltaic and optoelectronic devices, researchers have concentrated their efforts for the fundamental understanding of the ultrafast dynamics of the photo-generated carriers.

The ultrafast carrier dynamics of methylammonium lead halide perovskite ($MAPbX_3$, X=I, Br, Cl), which is the most well studied materials among the variety of HOIPs, have been studied by various optical techniques including terahertz (THz) time domain spectroscopy (THz-TDS),[11–17] optical Kerr spectroscopy,[18] transient absorption spectroscopy,[6,19–22] and time resolved photoluminescence.[3,6,21] From these studies, it is shown that the carrier recombination rates in HOIPs are unexpectedly low, manifesting the long charge carrier lifetime. There has been extensive discussion on the underlying physics of the slow recombination rates in HOIPs. Possible mechanisms are the polaronic effect,[18] photon recycling,[23] Rashba effect,[24] and energy exchange with trap states.[25] Among these mechanisms which more or less interplay with each other, the formation of polaronic states is considered to be of importance. In $MAPbBr_3$, the ultrafast deformation and equilibration of the lattice has been reported to finish within $\sim$ 1 ps after the photo-excitation, suggesting the formation of polaronic states.[18,19] Such ultrafast equilibrium process of the generated photo-carriers are followed by the various carrier recombination processes with different time scales ranging from several ps to hundreds of ns. Figure 1 shows schematics of typical carrier recombination pathways in semiconductors. When the carrier density is around the solar power level ($\sim 10^{15}$ cm^{-3}),

the principal recombination processes are the radiative bi-molecular recombination and trap-assisted recombination. As the carrier density gets higher, many-body collision process such as Auger-like recombination process becomes important.[26]

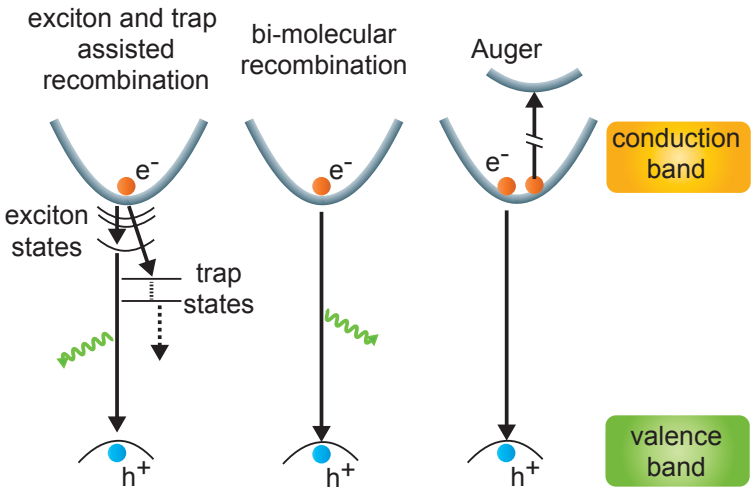

Figure 1:
Schematic illustration of various recombination pathways of free carriers in the conduction band.

It is known that the carrier recombination dynamics also depends on the band structure around the band edge.[27] In $MAPbI_3$, the exciton binding energy is reported to be around 10 – 20 meV which is comparable to the thermal energy at room temperature (RT). Therefore, it is considered that the generated bound excitons can generate free carriers by the absorption of thermal energy.[21,28–30] Such characteristics are of valuable for the photovoltaic applications because dissociated electrons and holes are necessary to generate photocurrents. Compared to $MAPbI_3$, the reported exciton binding energy of $MAPbBr_3$ is about 40 – 60 meV,[31] which is larger than the thermal energy at RT. Because of this, the probability for the excitons in $MAPbBr_3$ to form free carriers by the thermal energy is expected to be lower, so that ultrafast carrier response is expected to behave differently from $MAPbI_3$ when excited around the band-gap energy.

Up to now, there has been no report on the detailed analysis on the ultrafast carrier dynamics of $MAPbBr_3$ with the excitation energy carefully controlled around the band-edge

where excitons and free carriers are excited simultaneously. In this paper, we have applied the ultrafast THz-TDS to study the carrier dynamics in the sub-microcrystalline $MAPbBr_3$, especially focused on the exciton states formed by the resonant pump pulses. We focus our discussion on the rather fast decay processes up to 500 ps after the photo-carrier generation under the carrier density of $\sim 10^{18} - 10^{19}$ cm^{-3}. Therefore, the slow monomolecular radiative and non-radiative recombination and carrier diffusion processes occurring in nanosecond time scale are beyond the scope of our current research.

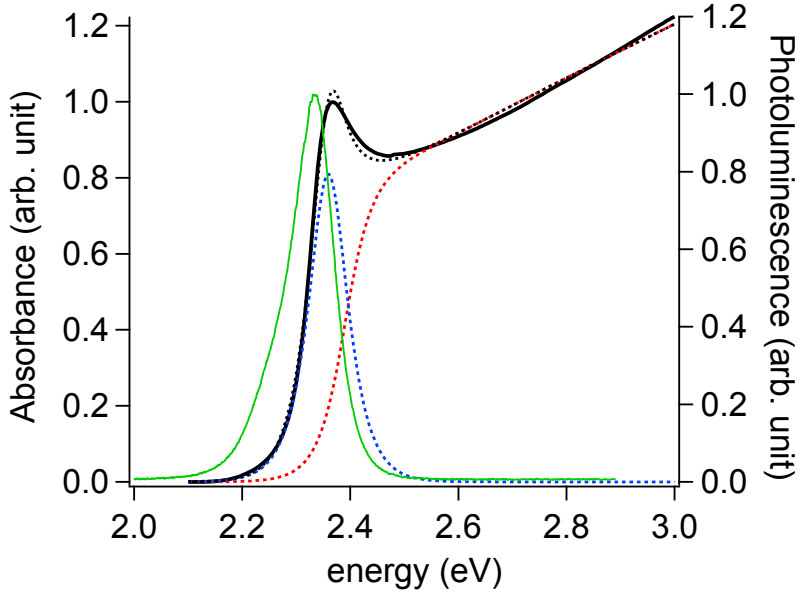

Figure 2:
Absorption (black) and photoluminescence (green) spectrum of $MAPbBr_3$ film with thickness of 250 nm. Black dotted line is the model calculation of absorption based on the Elliott's theory of Wannier excitons,[28,32] with its exciton and free carrier contributions given by blue and red dashed lines, respectively. See the Supporting Information for the details of the analysis.

A thin film of microcrystalline $MAPbBr_3$ is prepared by a solution-processed method.[2,19] The absorption and photoluminescence spectra measured at RT are shown in Fig. 2. Compared to the absorption spectrum of $MAPbI_3$,[23,30] the remarkable contribution of the exciton absorption around the band edge is clearly visible even at RT. The absorption spectrum is deconvolved into the exciton absorption and inter-band transitions based on the Elliott's theory of Wannier excitons.[28,32] Details of the analysis are explained in the Supporting In-

formation. Following the modelled absorption line-shape function, we plot the contribution of the exciton and free carrier components as shown in Fig. 2. From the fitting parameters, the binding energy of the $MAPbBr_3$ is derived to be 49.9 meV at RT, which agrees well with the value reported in previous papers.[31,33] The band gap of the $MAPbBr_3$ is derived to be 2.41 eV, which also agrees well with the reported absorption band gap of ~ 2.40 eV.[31,33] As expected, the binding energy of excitons in $MAPbBr_3$ allows the stable existence of photo-generated excitons at RT.

Optical pump-THz probe time-resolved measurements are performed to observe the temporal response of the photo-excited carriers and the THz transient conductivity spectrum. Details of the optical setup and measurement procedures are given in methods and in the Supporting Information. The amplitude of the transmitted THz pulse is estimated with the electro-optic (EO) sampling pulse whose timing is fixed to the first peak of the THz field amplitude. We have measured $\Delta E(t)/E(t)$ where $E(t)$ is the amplitude of input THz field, and $\Delta E(t)$ is the difference between input and transmitted THz field.[12] Keeping the timing of the EO sampling pulse fixed, we scan the timing of the pump pulse relative to the THz pulse. All the THz measurements are performed with a sample film of 180 nm thickness.

Figure 3(a) shows the transient THz transmittance $\Delta E(t)/E(t)$ at various pump fluences. The pump photon energy ϵ_{p} (wavelength) is fixed to 3.10 eV (400 nm) which is ~ 0.7 eV above the band gap. The temporal width of our THz pulse is ~ 2 ps, so that the ultrafast response related to the initial carrier cooling and polaron formation which are expected to occur within $t \leq 1$ ps cannot be resolved in our data.[19,34] Thus, we will focus our discussion on the decay process after the formation of the polaron states. Within the experimental delay up to $t \sim 500$ ps we have scanned, the dominant carrier relaxation processes are (i) Auger scattering process where an electron-hole pair recombines with their excess energy transferred to a third carrier, and (ii) radiative electron-hole pair recombination process. Other processes shown in Fig. 1, such as monomolecular trap-assisted recombination and photoluminescence from the exciton state occur at much longer timescale of ns to μs order

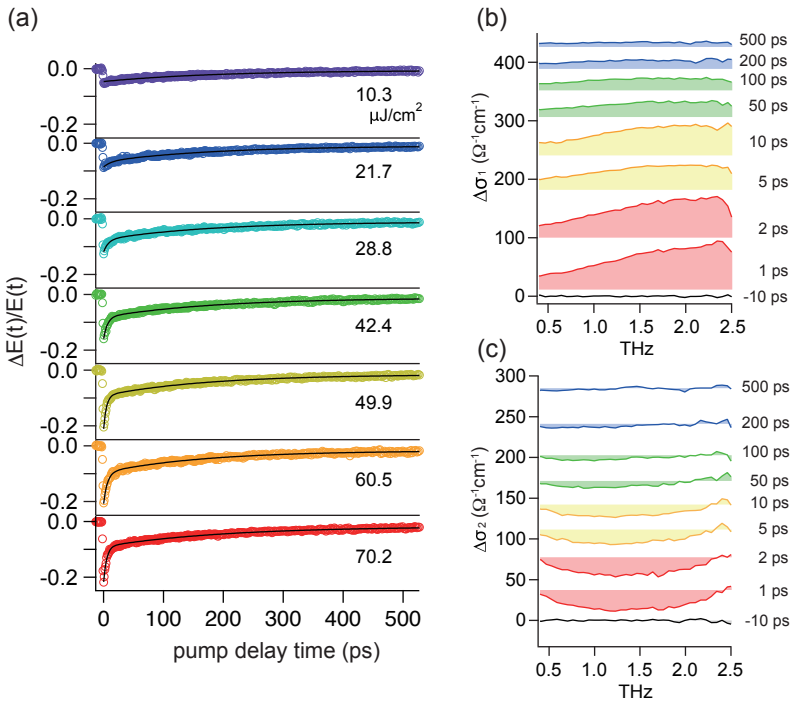

Figure 3:
(a) (Circles) Temporal evolution of THz electric field amplitude at different pump fluence. The pump photon energy (wavelength) is fixed to 3.10 eV (400 nm) which excites far from the band edge. (Black lines) Bi-exponential fit results except the data with 10.3 μJ/cm^2 which is fitted with a single exponential curve. (b),(c) Real and imaginary part of the THz transient conductivity induced by the pump pulse with 36.6 μJ/cm^2. Each data is offset vertically for clarity.

in HOIPs, so that their contribution is neglected in our current discussion.[21,25,28,35] This is a reasonable assumption considering the rather high pump fluence used in this experiment.[29] We have adopted two possible model functions to describe the observed temporal response of the THz electric field. The first model is a bi-exponential function given as

$$-\frac{\Delta E(t)}{E(t)} = A_{\mathrm{F}} \exp\left(-\frac{t-\tau_0}{\tau_{\mathrm{F}}}\right) + A_{\mathrm{S}} \exp\left(-\frac{t-\tau_0}{\tau_{\mathrm{S}}}\right) \tag{1}$$

where A_{X} and τ_{X} (X=F or S) are the amplitude and the time constant of the fast or slow component, respectively. The fitted bi-exponential curves are overlapped with the traces shown in Fig. 3(a). For the lowest fluence of 10.3 μJ/cm^2, the observed data is well fitted by a single exponential curve with the slow time constant. Therefore the value of A_{F} and τ_{F}

are not determined for this condition.

Figures 3(b) and (c) show the real and imaginary part of the THz transient conductivity ($\Delta\sigma = \Delta\sigma_1 + i\Delta\sigma_2$) spectrum measured with the fluence of 36.6 μJ/cm^2. It is clearly seen that the broad THz response appears immediately after the irradiation of the pump pulse. The broad THz conductivity spectrum and the negative contribution in the imaginary part are characteristic features for the Drude-Smith model of the conductivity in which the scattering of the free carriers by the defects is implemented.[12,16,36] These results support our analysis that the main contribution of the THz transient response is ascribed to free carrier dynamics, not to excitons. In $MAPbBr_3$, the low frequency phonon modes are reported at 1.35 and 2.19 THz.[13] In our sample, however, such peaks are buried in the broad response probably due to the thin film thickness of our sample and the inhomogeneous broadening at room temperature environment.

Another model to describe the carrier recombination dynamics is based on the carrier recombination rate equation given as[12,35]

$$\frac{dN(t)}{dt} = -k_3 N(t)^3 - k_2 N(t)^2 - k_1 N(t), \tag{2}$$

where $N(t)$ is the carrier density, and k_1, k_2 and k_3 are the monomolecular trap-assisted recombination, radiative bi-molecular recombination, and third-order Auger recombination rate coefficients, respectively. Here we assume $N(t)$ is related to our signal under the assumption that $N(t) \propto \frac{-\Delta E(t)}{E(t)}$. However, the fitting results (see the Supporting Information for details) do not reproduce the observed data compared to the bi-exponential function given by Eq. (1) especially under the high fluence condition. The reason for the failure of Eq. (2) may be ascribed to the contributions of other decay processes such as the non-radiative recombination through defects, scattering by the phonons, or the phonon bottleneck effect during the hot carrier cooling process.[37] It is reported that such phonon bottleneck effect slows down the hot carrier thermalization in $MAPbI_3$ under the high carrier density of 6.0

$\times 10^{18}\mathrm{cm}^{-3}$.[38] In our experiment, the estimated carrier density is $\sim 6.9 \times 10^{18}\mathrm{cm}^{-3}$ at the fluence of 70.2 $\mu\mathrm{J/cm}^2$, so it is reasonable to assume similar effect is important in $MAPbBr_3$. Thus in the following analysis, we will use Eq. (1) to discuss the decay process phenomenologically.

With the model function of Eq. (1), the resulting fitting parameters A_X and τ_X (X=F or S) for each pump fluence are summarized in Figs. 4(a) and (b). Both the A_F and τ_F seem to be saturated above the pump fluence of 50 $\mu\mathrm{J/cm}^2$. It is seen that the typical fast time constant τ_F is around 5 – 10 ps with slight decrease as the pump fluence increases. From Fig 4(b), again we see a saturating behavior of A_S above the pump fluence of 50 $\mu\mathrm{J/cm}^2$. The slow time constant τ_S is around 180 ps and almost constant over the whole range of the pump fluence. Fig. 4(c) shows the ratio of the amplitude A_F / A_S for each pump fluence. It is clearly seen that the fast response component is enhanced at higher pump fluence. From this result, we assign that the fast and slow response components represent the Auger-like three-body decay process and the bi-molecular electron-hole recombination process, respectively. It is reasonable to assume the three-body Auger process enhances under the high carrier density circumstances compared to the electron-hole recombination process, which is second-order dependent on the carrier density. The values of the time constants, τ_F (Auger-like) and τ_S (electron-hole) can be compared with the previous reports on similar materials. Cinquanta et al. has performed a similar THz-TDS with a film of nanocrystalline $CsPbBr_3$, and reported the time constants of $\sim$ 15 ps and hundreds of ps as two time constants of bi-exponential fitting curves, which are ascribed to Auger-like and band-to-band carrier recombination processes.[11] Zhu et al. reported the hot carrier luminescence decay lifetime of 160 ps for single crystalline $MAPbBr_3$.[3] The similar lifetime observed with different techniques supports our assignments for the fast and slow temporal responses. About the reason why τ_S does not accelerate with the increase of carrier density, it may be related to the slow carrier cooling due to the phonon bottleneck effect which hinders the immediate thermalization at the bottom of the conduction band.[37]

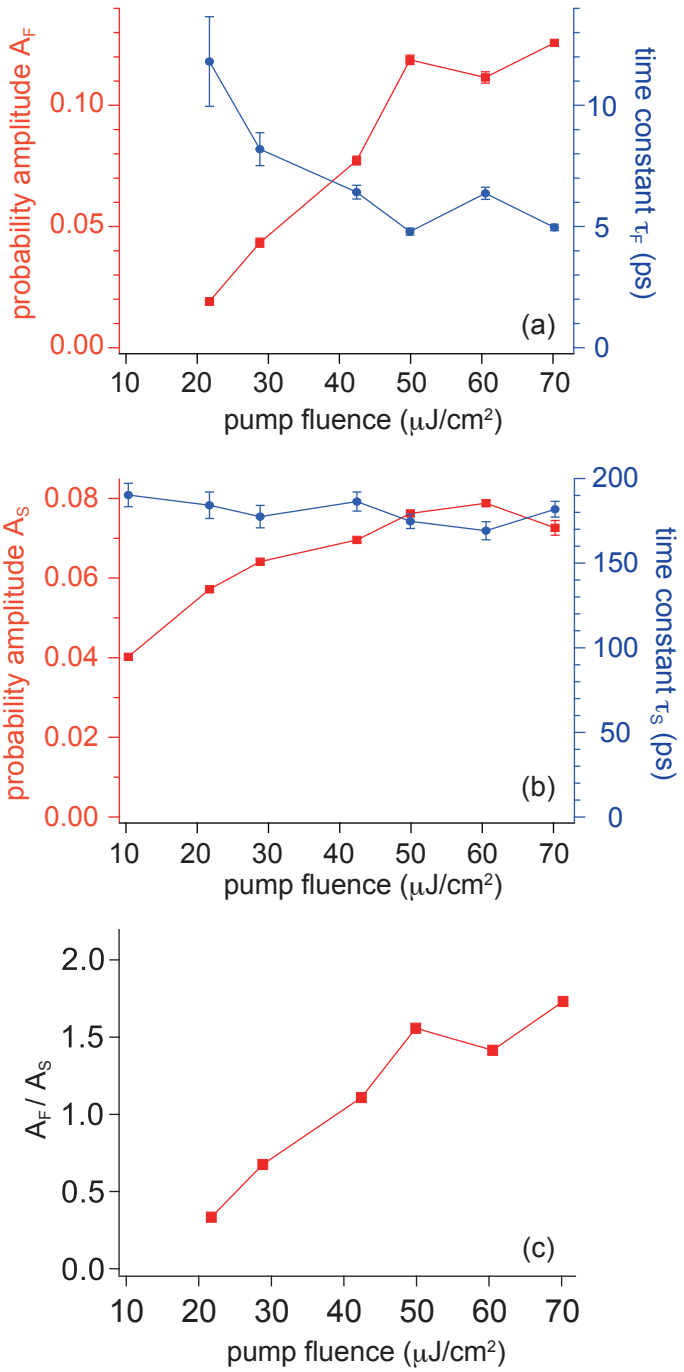

Figure 4:
(a) Pump fluence dependence of the amplitude (A_{F}) and time constant (τ_{F}) for the fast component. (b) Pump fluence dependence of the amplitude (A_{S}) and time constant (τ_{S}) for the slow component. For the fluence of 10.3 μJ/cm^2, the trace is well reproduced with a single exponential curve, so that A_{F} and τ_{F} are not defined. The error bar represents the 95% confidence interval of the fitted parameters. (c) Pump fluence dependence of the ratio of amplitude $A_{\mathrm{F}}/A_{\mathrm{S}}$.

The decrease in τ_{F} at the high pump fluence is expected to be related with the amplified spontaneous emission (ASE) process in the $MAPbBr_3$ crystal. Since the fluence of 50 μJ/cm^2 is above the ASE or lasing threshold of the typical $MAPbBr_3$ crystal,[3,39] the faster decay may be explained by the fast depopulation of the excited state triggered by the ASE process. Similar reduction of the relaxation lifetime at high pump fluence is reported in other highly luminescent organic and inorganic semiconductor materials in relation with the onset of the amplified spontaneous emission process.[40,41]

Next, we have observed the pump photon energy dependence of THz-TDS signal. We scan the central pump photon energy (wavelength) from $\epsilon_{\mathrm{p}} = 2.34$ eV (530 nm) to 2.46 eV (504 nm), while keeping the generated carrier density (n_0) constant. The details for the carrier density estimation are explained in the Supporting Information. The relation between the pump pulse spectra and the absorption line shape is shown in Fig. 5(a). By tuning ϵ_{p} from 2.34 to 2.46 eV, both bound excitons and inter-band transitions are excited with different ratio.

The observed THz-TDS results under the constant carrier density n_0 fixed to $\sim 1.0 \times 10^{19}$ cm^{-3} are plotted in Fig. 5(b). It is clearly seen that the temporal decay profile changes drastically depending on the photon energy of the pump pulse. The observed transient behavior are fitted with Eq. (1). The fitting parameters A_{X} and τ_{X} (X=F or S) for each pump photon energy are summarized in Fig. 5 (c) and (d). As a reference, the parameters obtained from the result in Fig. 3(a) with the pump fluence of 70.2 μJ/cm^2 ($\epsilon_{\mathrm{p}} = 3.10$ eV, $n_0 = 6.9 \times 10^{18}$ cm^{-3}) are plotted on the rightmost side. We can't set n_0 to the same value at $\epsilon_{\mathrm{p}} = 3.10$ eV due to the damage to the sample. For the condition of $\epsilon_{\mathrm{p}} = 2.34$ eV, the bi-exponential model is redundant so that we use a single exponential function corresponding to the slow response component to fit the observed data. The amplitude of the fast response component (A_{F}) decreases rapidly as the pump photon energy decreases and crosses the band-to-band transition edge. Meanwhile, the fast time constant (τ_{F}) shows no significant pump photon energy dependence and remains ~ 5 ps. The ratio of A_{F} at ϵ_{p}=2.36 and 2.46

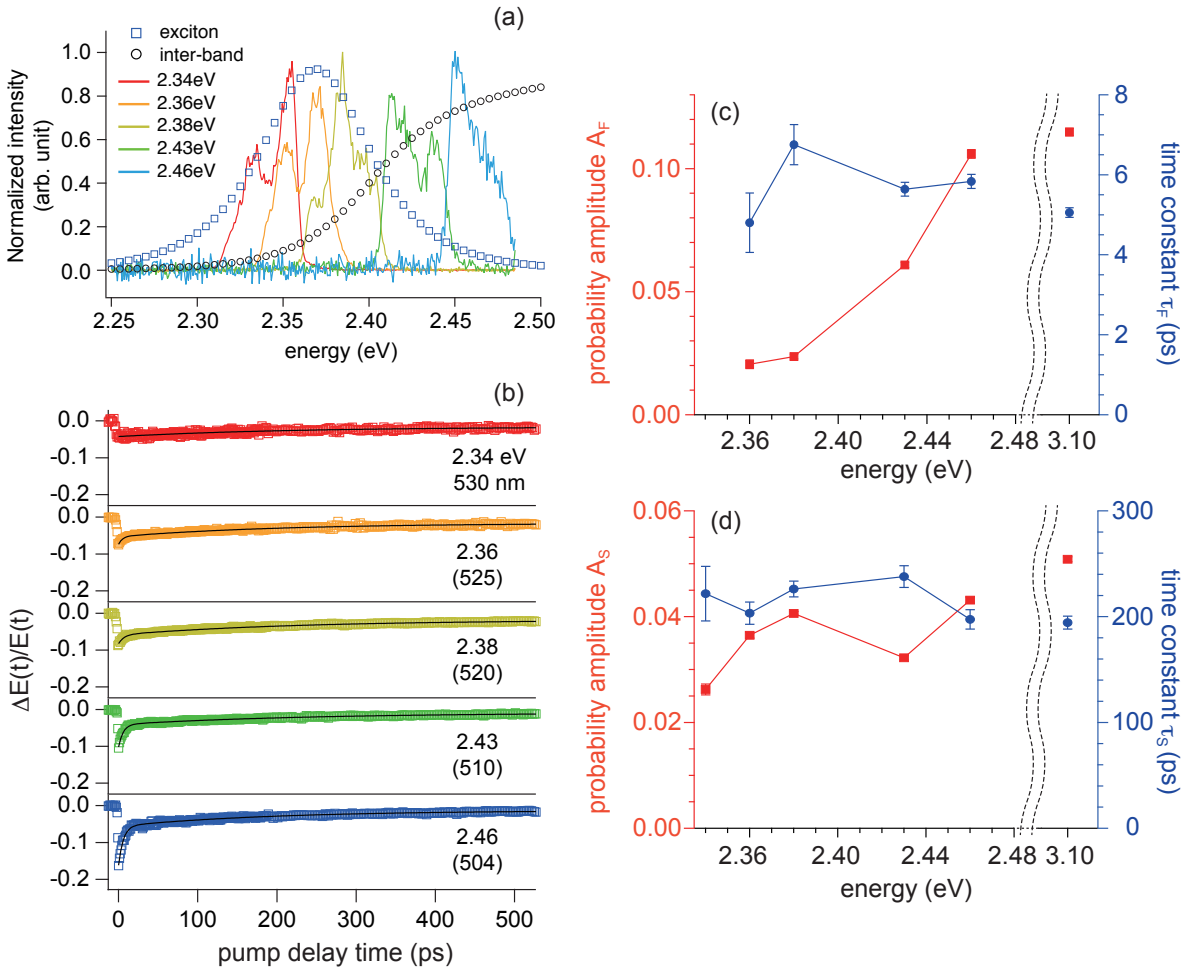

Figure 5:

(a) Normalized spectra of the pump pulse tuned from 2.34 to 2.46 eV. The exciton and inter-band transition profile shown in Fig. 2 is overlapped for reference. (b) (Squares) Temporal evolution of THz electric field amplitude at different pump photon energy. The generated carrier density n_0 is fixed to $\sim 1.0\times10^{19}$ cm^{-3}. (Black lines) Bi-exponential fit results except the data with 2.34 eV which is fitted with a single exponential curve. (c) Pump photon energy dependence of the amplitude ($A_{\rm F}$) and time constant ($\tau_{\rm F}$) for the fast component. (d) Pump photon energy dependence of the amplitude ($A_{\rm S}$) and time constant ($\tau_{\rm S}$) for the slow component. In (c) and (d), the result from Fig. 3(b) with pump fluence of 70 μJ/cm^2 ($\epsilon_{\rm p}$ = 3.10 eV and $n_0 = 6.9 \times 10^{18}$ cm^{-3}) is added for reference. For $\epsilon_{\rm p}$=2.34 eV, the trace is well reproduced with a single exponential curve, so that $A_{\rm F}$ and $\tau_{\rm F}$ are not defined. The error bar represents the 95% confidence interval of the fitted parameters.

eV is directly compared with the ratio of free carrier generated by the pump pulse. From the spectral profile shown in Fig. 5(a), we have estimated the population ratio P of the continuous band relative to the whole excitation (continuous band + exciton). The ratio P(2.46 eV)/P(2.36 eV) is 6.3, which is slightly larger than the ratio A_{F}(2.46 eV) / A_{F}(2.36 eV)= 5.2. This discrepancy may be related to the exciton bleach effect where the exciton oscillator strength is influenced by the population of free carriers.[42] More detailed studies, such as visible pump-white light probe experiment with carefully controlled pump photon energy will be needed to clarify such ultrafast modulation of the absorption by excitons and free carriers.[22] On the other hand, the photon energy dependence of the slow component A_{S} only slightly decreases as ϵ_{p} decreases. The observed decrease in A_{S} may be explained by the energy transfer to the nearby trap states at smaller ϵ_{p}, since these trapped states will not contribute to fast THz response. The τ_{S} is almost constant and comparable to ϵ_{p}=3.10 eV. This is reasonable assuming that the trapped states and exciton states do not contribute efficiently to the radiative recombination process up to 500 ps.

In the Auger recombination process, the recombination of electron and hole is accompanied by the excess energy and momentum transferred to the third carrier. From this picture, it is reasonable that such process is strongly suppressed when the stable exciton is generated in our microcrystalline film. Since the exciton state has only limited values of energy and momentum, the three-body scattering process satisfying the energy and momentum conservation simultaneously seems very difficult.[27,35] Unlike the nano-crystalline cases, the surface area to volume ratio is rather small in the current case, so that the accelerated surface Auger process is not expected. Another issue we should consider is the bi-exciton Auger recombination process in which two excitons collide with each other. From the estimated carrier density of $1.0\times\ 10^{19}$ cm^{-3} which is derived assuming 100% efficient carrier generation after photon absorption, the average exciton-exciton distance is calculated to be $\sim$ 6 nm which is on the same order as the reported exciton Bohr radius of $MAPbBr_3$.[43,44] However, we conclude such bi-exciton Auger scattering process is not efficient in the current measurement

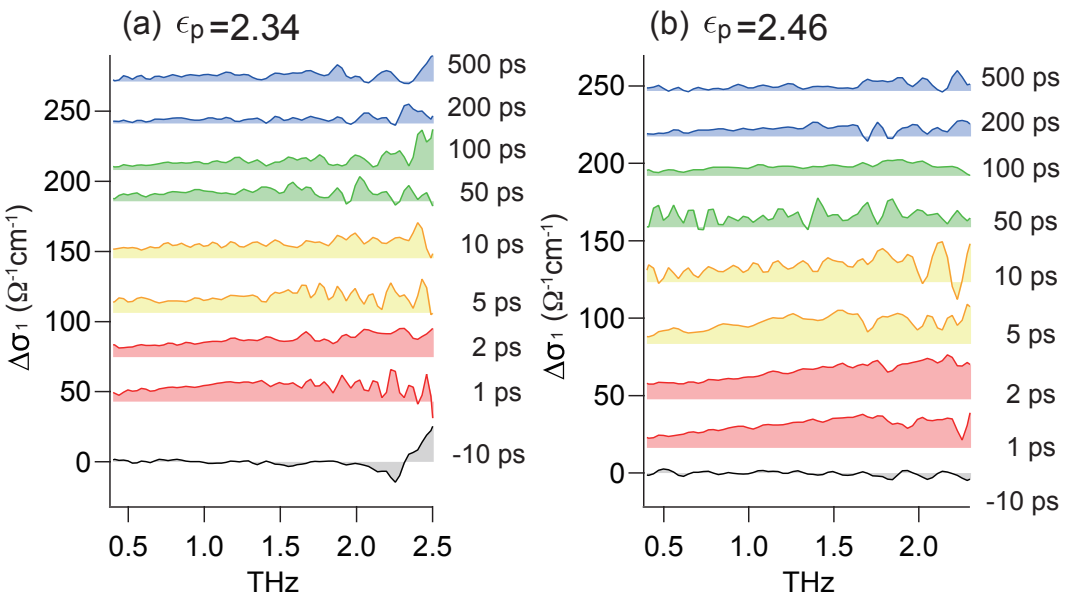

Figure 6:
(a) Real part of the THz transient conductivity spectrum with ϵ_p=2.34 eV. (b) Real part of the THz transient conductivity spectrum with ϵ_p=2.46 eV. Each data is offset vertically for clarity.

from following reasons. Firstly, the plot of τ_F given in Fig. 5 (c) does not show notable acceleration at the lower pump photon energy region where more portion of the pump photons is converted to the bound exciton state. Second, the observed temporal response at ϵ_p=2.34 eV has only a slow decay constant of $\sim$ 200 ps which is common to ϵ_p=3.10 eV. Thus the possibility that the fast decay component is ascribed to the bi-exciton Auger recombination is excluded in the current measurement. Together with the derived exciton binding energy of 49.9 meV, our THz-TDS measurement directly certifies that the excitons in $MAPbBr_3$ film stay as stable excitons at RT, which means that auto-ionization and re-formation of the excitons at the band edge is not important, unlike the situations observed in $MAPbI_3$.[21,28–30]

The real part of the THz transient conductivities measured with ϵ_p=2.34 and 2.46 eV is shown in Figs. 6 (a) and (b). The similar plots for the imaginary part are given in the Supporting Information Fig. S5. In both plots, broad frequency responses similar to the case ϵ_p=3.10 eV shown in Fig. 3(b) are observed while the amount of change is much smaller. Taking account of the different carrier density for ϵ_p=3.10 eV (3.6×10^{18} cm^{-3}) and 2.46, 2.34

eV (1.0×10^{19} cm^{-3}) experiment, the THz response with ϵ_p=3.10 eV is about one order of magnitude larger than ϵ_p= 2.46 and 2.34 eV cases. This is reasonable since the hot carrier distribution generated with ϵ_p=3.10 eV spreads more widely in the k-space compared to the other two cases. The similar broad spectral structure for three different ϵ_p also supports that the current THz response is originating mainly from the free carrier response, not due to the exciton absorption.

In our optical pump-THz probe measurements, the THz response is sensitive to the free carrier dynamics. Complimentarily, the dynamics of bound excitons can be directly accessed by optical pump-white light probe measurement.[20,45] We have checked using the same sample that the photo-bleach signal due to the bound exciton state is clearly observed at 2.35 eV with the lifetime longer than 500 ps.[45] From the rising edge of the exciton signal at three different pump photon energies (ϵ_p=3.10, 2.46 and 2.34 eV), it is clearly seen that the rise time takes longer for larger ϵ_p, reflecting the necessary hot carrier cooling time for higher ϵ_p. (See Supporting Information Fig. S6 for details.) These results support the stable existence of excitons, although they are not reflected to our transient THz response.

In conclusion, we have observed the pump fluence and photon energy dependent ultrafast carrier dynamics in $MAPbBr_3$ thin film by ultrafast THz-TDS. From the pump fluence dependence of the THz field amplitude, the relaxation dynamics within 500 ps after the photo excitation is explained by the contribution of two recombination processes, the fast Auger recombination and the relatively slow radiative bi-molecular recombination. From the pump photon energy dependence close to the band-gap energy, we have observed drastic decrease of the contribution of Auger recombination under the constant absorption photon density. This result supports that the populated exciton states in $MAPbBr_3$ which has $\sim$ 50 meV binding energy remain stable at RT. These results are contrastive to the cases in $MAPbI_3$ in which the populations of the bound exciton state are thermally excited to the free carrier states at RT. The strong inhibition of the Auger-like process in $MAPbBr_3$ when excited at the band gap energy will help to understand the carrier dynamics around the

band edge, which may contribute for the design of HOIP based devices for future photonic device applications.[46]

Acknowledgement

The authors thank Mr. S. Katao (Nara Institute of Science and Technology) for helping the X-ray diffraction measurements. This work was supported by JSPS KAKENHI (Grant No. 18H01900).

Supporting Information Available: Sample preparation and evaluation, details of optical setup, details of signal analysis procedures, estimation of generated carrier density, pump intensity distribution along the depth direction, $\Delta\sigma_2$ plots for ϵ_{p}=2.34 and 2.46 eV, and optical pump-white light probe measurement of excitons. Figures S1-S6; and Table S1, S2 (PDF).

Experimental section

Sample preparation and evaluation

A 1 mm-thick quartz substrate was cleaned with acetone, and treated with UV-ozone cleaning for 20 min. Methylammonium bromide (MABr) and Lead(II) bromide ($PbBr_2$) (purchased from Wako Pure Chemical Industries, Ltd.) were mixed with 1:1 molar ratio, and dissolved in a mixture of N,N-dimethylformamide (DMF) / dimethyl sulfoxide (DMSO) (4:1 volume ratio) with 30 wt% concentration. This precursor solution was spin coated on a quartz substrate. The conditions of spin coat was 1000 rpm for 10 s, followed by 4000 rpm for 30 s. During the 4000 rpm rotation, we dripped 250 μl of chlorobenzene. After the coating process, the sample was annealed at 80°C for 5 min, and successively annealed at 100°C for 10 min. The thickness of the film used for the THz measurement is estimated to be $\sim$ 180 nm by a mechanical profilometer. For the absorption and photoluminescence measurement,

we used another sample with $\sim$ 250 nm thickness, which was prepared with slightly different conditions. (30 $\rightarrow$ 40 wt%, 4000 $\rightarrow$ 3000 rpm, 250 $\rightarrow$ 100 μl.) The typical sample image by scanning electron microscope and X-ray diffraction patterns are available in the Supporting Information Fig. S1.

THz measurement scheme

To measure the ultrafast carrier dynamics with THz pulses, a THz-TDS is applied in this study.[47–55] Ti:Sapphire regenerative and subsequent multi-pass amplifiers were employed to generate pulses with a center wavelength of 800 nm, a pulse duration of 55 fs, and a pulse energy of 2 mJ at 1 kHz repetition rate. The amplified pulse was split into three parts for THz light generation, EO sampling, and optical pumping of the sample. The THz pulse was generated by optical rectification in a ZnTe crystal with a thickness of 1 mm. The pump pulse energy for the THz light generation was 0.3 mJ. The THz pulse was focused on the sample with a spot size of 2 mm in diameter, which was sufficiently smaller than that of the optical pump pulse mentioned later. The transmitted THz pulse from the sample was collimated and focused on the second ZnTe crystal for the EO sampling of the THz pulse. The EO sampling pulse was focused on the second ZnTe crystal irradiated by the THz pulse. The polarization state of the EO sampling pulse transmitted from the ZnTe crystal was measured by a balanced detection system. The birefringence due to the EO effect in the ZnTe crystal irradiated by the THz pulse linearly depends on the amplitude of the THz electric field, and changes the polarization state of the EO sampling pulse. The optical delay of the EO sampling pulse was scanned to trace the THz waveform. The schematic diagram of our experimental apparatus is shown in Fig. S2 together with the example of THz waveform and its Fourier transformed spectrum.

The optical pump pulse was prepared by two ways. To generate the UV pump pulse with a wavelength of 400 nm, the Ti:Sapphire output was frequency doubled by a 1-mm-thick β-BBO crystal. The wavelength-tunable visible pulse was generated by the sum-frequency

generation with a 1-mm-thick β-BBO crystal between the Ti:Sapphire output and the signal or idler output from an optical parametric amplifier (Light Conversion, TOPAS). A narrow bandpass filter (Thorlabs FLH532-10) was used to get spectrally narrowed pump pulse. The pump photon energy was tuned by slightly tilting the incidence angle of the filter. The pulse width after the band pass filter was measured with second-harmonic generation autocorrelation, and its full width at half maximum was $\sim$ 230 fs at 2.34 eV and $\sim$ 150 fs at 2.46 eV.

Data collection protocol

The time-dependence of the THz transmittance from the sample (see Fig. 3(a) and Fig. 5(b)) was measured by scanning the optical delay τ between the THz pulse and the optical pump pulse. In this measurement, the optical delay of the EO sampling pulse was fixed at the maximum amplitude of the THz waveform where the time was zero in the Fig. S2(b). To realize the quantitative analysis of the decay profiles and the time-dependent conductivity spectra, we employed the boxcar averaging of the signal from the balanced detector (PDB450A, Thorlabs) with a data acquisition (DAQ) device (USB-6210, National Instruments). The THz pulse and the optical pump pulse were chopped at the frequency of 500 Hz and 250 Hz (MC2000, Thorlabs), respectively. Each data was averaged 100 times to improve the signal-to-noise ratio further. The transient conductivity at τ was measured by obtaining the whole THz field profile by scanning the delay between the THz pulse and the EO sampling pulse. From the observed THz field transmittance with and without the pump pulse, we have calculated the transient conductivity shift $\Delta\sigma(\tau)$ following the equation valid for thin film samples on a THz-transparent substrate given as,[56]

$$\Delta\sigma(\tau) = -\epsilon_0 \frac{c}{d}(1 + n_{\mathrm{sub}}) \frac{\Delta E(\tau)}{E(\tau)}, \tag{3}$$

where the parameter ϵ_0, c, d, and n_{sub} are the vacuum permittivity, speed of light in vacuum, sample thickness, and the refractive index of the quartz substrate. We use the constant value of n_{sub}=2.09[57] for the analysis.

References

(1) Kojima, A.; Teshima, K.; Shirai, Y.; Miyasaka, T. Organometal Halide Perovskites as Visible-Light Sensitizers for Photovoltaic Cells. *J. Am. Chem. Soc.* **2009**, *131*, 6050–6051.

(2) Lee, M. M.; Tescher, J.; Miyasaka, T.; Murakami, T. N.; Snaith, H. J. Efficient Hybrid Solar Cells Based on Meso-Superstructured Organometal Halide Perovskites. *Science* **2012**, *338*, 643–647.

(3) Zhu, H.; Fu, Y.; Meng, F.; Wu, X.; Gong, Z.; Ding, Q.; Gustafsson, M. V.; Trinh, M. T.; Jin, S.; Zhu, X.-Y. Lead halide perovskite nanowire lasers with low lasing thresholds and high quality factors. *Nat. Mater.* **2015**, *14*, 636–642.

(4) Xing, G.; Mathews, N.; Lim, S. S.; Yantara, N.; Liu, X.; Sabba, D.; Grätzel, M.; Mhaisalkar, S.; Sum, T. C. Low-temperature solution-processed wavelength-tunable perovskites for lasing. *Nat. Mat.* **2014**, *13*, 476–480.

(5) Jia, Y.; Kerner, R. A.; Grede, A. J.; Rand, B. P.; Giebink, N. C. Continuous-wave lasing in an organic-inorganic lead halide perovskite semiconductor. *Nat. Photon.* **2017**, *11*, 784–789.

(6) Deschler, F.; Price, M.; Pathak, S.; Klintberg, L. E.; Jarausch, D.-D.; Higler, R.; Hüttner, S.; Leijtens, T.; Stranks, S. D.; Snaith, H. J.; Atatüre, M.; Phillips, R. T.; Friend, R. H. High Photoluminescence Efficiency and Optically Pumped Lasing in Solution-Processed Mixed Halide Perovskite Semiconductors. *J. Phys. Chem. Lett.* **2014**, *5*, 1421–1426.

(7) Tan, Z.-K.; Moghaddam, R. S.; Lai, M. L.; Docampo, P.; Higler, R.; Deschler, F.; Price, M.; Sadhanala, A.; Pazos, L. M.; Credgington, D.; Hanusch, F.; Bein, T.; Snaith, H. J.; Friend, R. H. Bright light-emitting diodes based on organometal halide perovskite. *Nat. Nanotechnol.* **2014**, *9*, 687–692.

(8) Cho, H.; Jeong, S.-H.; Park, M.-H.; Kim, Y.-H.; Wolf, C.; Lee, C.-L.; Heo, J. H.; Sadhanala, A.; Myoung, N.; Yoo, S.; Im, S. H.; Friend, R. H., Lee, T.-W. Overcoming the electroluminescence efficiency limitations of perovskite light-emitting diodes. *Science* **2015**, *350*, 1222–1225.

(9) Lin, K.; Xing, J.; Quan, L. N.; de Arquer, F. P. G.; Gong, X.; Lu, J.; Xie, L.; Zhao, W.; Zhang, D.; Yan, C.; Li, W.; Liu, X.; Lu, Y.; Kirman, J.; Sargent, E. H.; Xiong, Q.; Wei, Z. Perovskite light-emitting diodes with external quantum efficiency exceeding 20 per cent. *Nature* **2018**, *562*, 245-248.

(10) Mcmeekin, D. P.; Sadoughi, G.; Rehman, W.; Eperon, G. E.; Saliba, M.; Hörantner, M. T.; Haghighirad, A.; Sakai, N.; Korte, M.; Rech, B.; Johnston, M. B.; Herz, L. M.; Snaith, H. J. A mixed-cation lead mixed-halide perovskite absorber for tandem solar cells. *Science* **2016**, *351*, 151–155.

(11) Cinquanta, E.; Meggiolaro, D., Motti, S. G.; Gandini, M.; Alcocer, M. J. P.; Akkerman, Q. A.; Vozzi, C.; Manna, L.; Angelis, F. D.; Petrozza, A.; Stagira, S. Ultrafast THz Probe of Photoinduced Polarons in Lead-Halide Perovskites. *Phys. Rev. Lett.* **2019**, *122*, 166601.

(12) Zhao, D.; Chia, E. E. M. Free Carrier, Exciton, and Phonon Dynamics in Lead-Halide Perovskites Studied with Ultrafast Terahertz Spectroscopy. *Adv. Opt. Matt.* **2019**, *8*, 1900783.

(13) Zhao, D.; Skelton, J. M.; Hu, H.; La-o-vorakiat, C.; Zhu, J.-X.; Markus, R. A.; Michel-Beyerle, M-E.; Lam, Y. M.; Walsh, A.; Chia, E. E. M. Low-frequency optical phonon

modes and carrier mobility in the halide perovskite $CH_3NH_3PbBr_3$ using terahertz time-domain spectroscopy. *Appl. Phys. Lett.* **2017**, *111*, 201903.

(14) Yettapu, G. R.; Talukdar, D.; Sarkar, S.; Swarnkar, A.; Nag, A.; Ghosh, P.; Mandal, P. Terahertz Conductivity within Colloidal $CsPbBr_3$ Perovskite Nanocrystals: Remarkably High Carrier Mobilities and Large Diffusion Lengths. *Nano Lett.* **2016**, *16*, 4838–4848.

(15) Rehman, W.; Milot, R. L.; Eperon, E.; Wehrenfennig, C.; Boland, J. L.; Snaith, H. J.; Johnston, M. B.; Herz, L. M. Charge-Carrier Dynamics and Mobilities in Formamidinium Lead Mixed-Halide Perovskites. *Adv. Mater.* **2015**, *27*, 7938–7944.

(16) La-o-vorakiat, C.; Salim, T.; Kadro, J.; Khuc, M.-T.; Haselsberger, R.; Cheng, L.; Xia, H.; Gurzadyan, G. G.; Su, H.; Lam, Y. M.; Marcus, R. A.; Michel-Beyerle, M.-E.; Chia, E. E. M. Elucidating the role of disorder and free-carrier recombination kinetics in $CH_3NH_3PbI_3$ perovskite films. *Nat. Commun.* **2015**, *6*, 7903.

(17) Luo, L.; Men, L.; Liu, Z.; Mudryk, Y.; Zhao, X., Yao, Y., Park, J. M.; Shinar, R.; Shinar, J.; Ho, K.-M., Perakis, I. E., Vela, J.; Wang, J. Ultrafast terahertz snapshots of excitonic Rydberg states and electronic coherence in an organometal halide perovskite. *Nat. Commun.* **2017**, *8*, 15565.

(18) Miyata, K.; Atallah, T. L.; Zhu, X.-Y. Lead halide perovskites: Crystal-liquid duality, phonon glass electron crystals, and large polaron formation. *Sci. Adv.* **2017**, *3*, e1701469.

(19) Batignani, G.; Fumero, G.; Kandara, A. R. S.; Cerullo, G.; Gandini, M.; Ferrante, C.; Petrozza, A.; Scopigno, T. Probing femtosecond lattice displacement upon photo-carrier generation in lead halide perovskite. *Nat. Commun.* **2018**, *9*, 1971.

(20) Price, M. B.; Butkus, J.; Jellicoe, T. C.; Sadhanala, A.; Briane, A.; Halpert, J. E.; Broch, K.; Hodgkiss, J. M.; Friend, R. H.; Deschler, F. Hot-carrier cooling and pho-

toinduced refractive index changes in organic-inorganic lead halide perovskites. *Nat. Commun.* **2015**, *6*, 8420.

(21) Yamada, Y.; Nakamura, T.; Wakamiya, A.; Kanemitsu, Y. Photocarrier Recombination Dynamics in Perovskite $CH_3NH_3PbI_3$ for Solar Cell Applications. *J. Am. Chem. Soc.* **2014**, *136*, 11610-11613.

(22) Sharma, V.; Aharon, S.; Gdor, I.; Yang, C.; Etgar, L.; Ruhman, S. New insights on exciton binding and relaxation from high time resolution ultrafast spectroscopy of $CH_3NH_3PbI_3$ and $CH_3NH_3PbBr_3$ films *J. Mater. Chem. A* **2016**, *4*, 3546 – 3553.

(23) Richter, J. M.; Abdi-Jalebi, M.; Sadhanala, A.; Tabachnyk, M.; Rivett, J. P. H.; Pazos-Outón, L. M.; Gödel, K. C.; Proce, M.; Deschler, F.; Friend, R. H. Enhancing photoluminescence yields in lead halide perovskites by photon recycling and light out-coupling. *Nat. Commun.* **2016**, *7*, 13941.

(24) Niesner, D; Wilhelm, M.; Levchuk, I.; Osvet, A.; Shrestha, S.; Batentschuk, M.; Brabec, C.; Fauster, T. Giant Rashba Splitting in $CH_3NH_3PbBr_3$ Organic-Inorganic Perovskite. *Phys. Rev. Lett.* **2016**, *117*, 126401.

(25) deQuilettes, D. W.; Frohna, K.; Emin, D.; Kirchartz, T.; Bulovic, V.; Ginger, D. S.; Stranks, S. D. Charge-Carrier Recombination in Halide Perovskites. *Chem. Rev.* **2019**, *119*, 11007–11019.

(26) Johnston, M. B.; Herz, L. M. Hybrid Perovskites for Photovoltaics: Charge-Carrier Recombination, Diffusion, and Radiative Efficiencies. *Acc. Chem .Res.* **2016**, *49*, 146–154.

(27) Kulkarni, S. A.; Yantara, N.; Tan, K. S.; Mathews, N.; Mhaisalkar, S. G. Perovskite nanostructures: Leveraging quantum effects to challenge optoelectronic limits. *Mater. Today* **2020**, *33*, 122–140.

(28) Saba, M.; Cadelano, M.; Marongiu, D.; Chen, F.; Valerio, S.; Sestu, N.; Figus, C.; Aresti, M.; Piras, R.; Lehmann, A. G.; Cannas, C.; Musinu, A.; Quochi, F.; Mura, A.; Bongiovanni, G. Correlated electron-hole plasma in organometal perovskites. *Nat. Commun.* **2014**, *5*, 5049.

(29) Wehrenfennig, C.; Eperon, G. E.; Johnston, M. B.; Snaith, H. J.; Herz, L. M. High Charge Carrier Mobilities and Lifetimes in Organolead Trihalide Perovskites. *Adv. Mater.* **2014**, *26*, 1584–1589.

(30) Chen, X.; Lu, H.; Yang, Y.; Beard, M. C. Excitonic Effects in Methylammonium Lead Halide Perovskites. *J. Phys. Chem. Lett.* **2018**, *9*, 2595–2603.

(31) Yang, Y.; Yang, M.; Li, Z.; Crisp, R.; Zhu, K.; Beard, M. C. Comparison of Recombination Dynamics in $CH_3NH_3PbBr_3$ and $CH_3NH_3PbI_3$ Perovskite Films: Influence of Exciton Binding Energy. *J. Phys. Chem. Lett.* **2015**, *6*, 4688–4692.

(32) Elliott, R. J. Intensity of optical absorption by excitons. *Phys. Rev.* **1957**, *108*, 1384–1389.

(33) Wolf, C.; Kim, J-S.; Lee, T-W. Structural and Thermal Disorder of Solution-Processed $CH_3NH_3PbBr_3$ Hybrid Perovskite Thin Films. *Appl. Mater. Interfaces* **2017**, *9*, 10344–10348.

(34) Niesner, D.; Zhu, H.; Miyata, K.; Joshi, P. P.; Evans, T. J. S.; Kudisch, B. J.; Trinh, M. T. Marks, M.; Zhu, X.-Y. Persistent Energetic Electrons in Methylammonium Lead Iodide Perovskite Thin Films. *J. Am. Chem. Soc.* **2016**, *138*, 15717–15726.

(35) Herz, L. M. Charge-Carrier Dynamics in Organic-Inorganic Metal Halide Perovskites. *Annu. Rev. Phys. Chem.* **2016**, *67*, 65–89.

(36) Smith, N. V.; Classical generalization of the Drude formula for the optical conductivity. *Phys. Rev. B* **2001**, *64*, 155106.

(37) Klimov, V.; Bolivar, P. H.; Kurz, H. Hot-phonon effects in femtosecond luminescence spectra of electron-hole plasmas in CdS. *Phys. Rev. B* **1995**, *52*, 4728–4731.

(38) Yang, Y.; Ostrowski, D. P.; France, R. M.; Zhu, K.; van de Lagemaat, L.; Luther, J. M.; Beard, M. C. Observation of a hot-phonon bottleneck in lead-iodide perovskites. *Nat. Photon.* **2016**, *10*, 53–59.

(39) Nguyen, V.-C.; Katsuki, H.; Sasaki, F.; Yanagi, H. Optically pumped lasing in single crystals of organometal halide perovskites prepared by cast-capping method. *Appl. Phys. Lett.* **2016**, *108*, 261105.

(40) Mizuno, H.; Maeda, T.; Yanagi, H.; Katsuki, H.; Aresti, M.; Quochi, F.; Saba, M.; Mura, A.; Bongiovanni, G.; Sasaki, F.; Hotta, S. Optically Pumped Lasing from Epitaxially Oriented Needle Crystals of a Thiophene/Phenylene Co-Oligomer. *Adv. Mater.* **2012**, *24*, 529-534.

(41) Xhang, Q.; Liu, X.; Utama, M. I. B.; Zhang, J.; de la Mata, M.; Arbiol, J.; Lu, Y.; Sum, T. C.; Xiong, Q. Highly Enhanced Exciton Recombination Rate by Strong Electron Phonon Coupling in Single ZnTe Nanobelt. *Nano Lett.* **2012**, *12*, 6420-6427.

(42) Huang, D.; Chyi, J.-I.; Morkoç, H. Carrier effects on the excitonic absorption in GaAs quantum-well structures: Phase-space filling. *Phys. Rev. B* **1990**, *42*, 5147 – 5153.

(43) Tanaka, K.; Takahashi, T.; Ban, T.; Kondo, T.; Uchida, K.; Miura, N. Comparative study on the excitons in lead-halide-based perovskite-type crystals $CH_3NH_3PbBr_3$ $CH_3NH_3PbI_3$. *Solid State Commun.* **2003**, *127*, 619–623.

(44) Baranowski, M.; Galkowski, K.; Surrente, A.; Urban, J.; Klopotowski, Ł.; Maćkowski, S.; Maude, D. K.; Aich, R. B.; Boujdaria, K.; Chamarro, M.; Testelin, C.; Nayak, P. K.; Dollmann, M.; Snaith, H. J.; Nicholas, R. J.; Plochocka, P. Giant Fine Structure Splitting of the Bright Exciton in a Bulk $MAPbBr_3$ Single Crystal, *Nano Lett.* **2019**, *19*, 7054–7061.

(45) Grancini, G.; Kandada, A. R. S.; Frost, J. M.; Barker, A. J.; De Bastiani, M.; Gandini, M.; Marras, S.; Lanzani, G.; Walsh, A.; Petrozza, A. Role of microstructure in the electron-hole interaction of hybrid lead halide perovskites. *Nat. Photon.* **2015**, *9*, 695-702.

(46) Wei, C.; Chen, X.; Li, D.; Su, H,; He, H.; Dai, J.-F. Bound exciton and free exciton states in GaSe thin slab. *Sci. Rep.* **2016**, *6*, 33890.

(47) Guillet, J.P.; Recur, B.; Frederique, L.; Bousquet, B.; Canioni, L.; Manek-Honninger, I.; Desbarats, P.; Mounaix, P. Review of terahertz tomography techniques. J. Infrared Millim. Terahertz Waves **2104**, *35*, 382 - 411.

(48) Fitzgerald, A.J.; Berry, E.; Zinovev, N.N.; Walker, G.C.; Smith, M.A.; Chamberlain, J.M. An introduction to medical imaging with coherent terahertz frequency radiation. Phys. Med. Biol. **2002**, *47*, R67-R84.

(49) Kulya, M.; Petrov, N.V.; Tsypkin, A.; Egiazarian, K.; Katkovnik, V. Hyperspectral data denoising for terahertz pulse time-domain holography. Opt. Express **2019**, *27*, 18456-18476.

(50) Aghamiri, N.A.; Huth, F.; Huber, A.J.; Fali, A.; Hillenbrand, R.; Abate, Y. Hyperspectral time-domain terahertz nano-imaging. Opt. Express **2019**, *27*, 24231-24242.

(51) Zhang, X.C. Three-dimensional terahertz wave imaging. Phil. Trans. R. Soc. Lond. A **2004**, *362*, 283-298.

(52) Son, J.-H. *Terahertz biomedical science and technology.*; CRC Press: Boca Raton, FL, USA, 2014.

(53) Song, H.-J.; Nagatsuma, T. *Handbook of terahertz technologies: Devices and applications.* Jenny Stanford Publishing: New York, NY, USA, 2015.

(54) Tsubouchi, M.; Nagai, M.; Ohshima, Y. Terahertz tomography of a photo-induced carrier based on pump-probe spectroscopy using counterpropagation geometry. *Opt. Lett.* **2012**, *37*, 3528–3530.

(55) Kohno, N.; Itakura, R.; Tsubouchi, M. Mechanism of relativistic Doppler reflection from a photoinduced moving plasma front studied by terahertz time-domain spectroscopy. *Phys. Rev. B* **2016**, *94*, 155205.

(56) La-o-vorakiat, C.; Cheng, L.; Salim, T.; Marcus, R. A.; Michel-Beyerle, M.-E.; Lam, Y. M.; Chia, E. E. M. Phonon features in terahertz photoconductivity spectra due to data analysis artifact: A case study on organometallic halide perovskites. *Appl. Phys. Lett.* **2017**, *110*, 123901.

(57) Davies, C. L.; Patel, J. B.; Xia, C. Q.; Herz, L. M.; Johnston, M. B. Temperature-Dependent Refractive Index of Quartz at Terahertz Frequencies. *J. Infrared Millim. Terahertz Waves* **2018**, *39*, 1236-1248.